

# Signature of Mesoscale Eddies on Air-Sea Heat Fluxes in the North Indian Ocean

Yanxu Chen<sup>1</sup>  and Lisan Yu<sup>1</sup> 

<sup>1</sup>Department of Physical Oceanography, Woods Hole Oceanographic Institution, Woods Hole, MA, USA

### Key Points:

- Eddy-induced SST-THF coefficient can approach  $\sim 40$  and  $\sim 28 \text{ W m}^{-2} \text{ k}^{-1}$  for warm anticyclones and cold cyclones
- SSH-SST incoherent eddies (warm cyclones and cold anticyclones) are comparable in number to coherent/conventional eddies
- Seasonal variation of eddy compositions leads to monopolar, dipolar and canceled patterns of air-sea net fluxes

### Correspondence to:

Y. Chen,  
[yanxu.chen@whoi.edu](mailto:yanxu.chen@whoi.edu)

### Citation:

Chen, Y., & Yu, L. (2024). Signature of mesoscale eddies on air-sea heat fluxes in the North Indian Ocean. *Journal of Geophysical Research: Oceans*, 129, e2023JC019878. <https://doi.org/10.1029/2023JC019878>

Received 31 MAR 2023

Accepted 25 FEB 2024

### Author Contributions:

**Conceptualization:** Yanxu Chen, Lisan Yu

**Funding acquisition:** Lisan Yu

**Methodology:** Yanxu Chen, Lisan Yu

**Resources:** Lisan Yu

**Supervision:** Lisan Yu

**Validation:** Yanxu Chen, Lisan Yu

**Visualization:** Yanxu Chen

**Writing – original draft:** Yanxu Chen

**Writing – review & editing:** Lisan Yu

**Abstract** Using a combination of 20-year (1999–2018) remotely-sensed air-sea heat flux products and altimeter-based eddy atlas, we investigate the signature of mesoscale eddies on sea surface temperature (SST) and air-sea turbulent latent and sensible fluxes, or simply, turbulent heat fluxes (THFs), in the North Indian Ocean. On average, eddy-induced THF feedback can approach  $\sim 40 \text{ W m}^{-2} \text{ k}^{-1}$  for warm-core anticyclones (AEs) and  $\sim 28 \text{ W m}^{-2} \text{ k}^{-1}$  for cold-core cyclones (CEs) at their extreme values. In addition to these conventional SSH-SST coherent eddies and their imprints as monopoles in heat fluxes, a comparable proportion of SSH-SST incoherent eddies (cold-AEs and warm-CEs) are surprisingly active in this region, which offset the monopolar paradigm of coherent eddy-induced THF anomalies or develop a dipole structure when combined with these conventional eddies. In terms of seasonality, the aggregation of SSH-SST coherent and incoherent eddies in the Arabian Sea develops concentrated monopoles within eddy contours in both summer and winter, with a damped THF located farther away from the eddy core in winter. In the Bay of Bengal, a strong compensation between SSH-SST coherent and incoherent eddies is observed in summer that leads to null net fluxes, while the winter-time THF composite of these two eddy types displays a dipolar structure which was described as eddy-stirring effect in the literature.

**Plain Language Summary** The typical turbulent feature of the ocean surface, as depicted from satellite images, is often referred to as eddies that are crucial to the evolution of ocean states under climate change. With two data sources, both of which originate from satellite-based derivations, we investigate how mesoscale eddies (with spatiotemporal scales of  $\sim 100 \text{ km}$  and  $\sim 1 \text{ month}$ ) contribute to air-sea heat exchanges and related processes in the North Indian Ocean. The seasonality of sea surface conditions is of great importance to behaviors and proportions of different eddy types in this region. Specifically, unconventional eddies, characterized as cold-core anticyclones and warm-core cyclones, are surprisingly active in the Arabian Sea and Bay of Bengal. This atypical feature implies that a thorough integration of dynamic and thermodynamic processes in understanding the ocean mesoscale is necessary.

## 1. Introduction

The well-accepted weather system of the ocean—mesoscale eddies—is typically formed due to instabilities of strongly sheared flows at the western boundary or current-topography interactions (Abernathey & Cessi, 2014; Barthel et al., 2022; Vic et al., 2015). Other theories of eddy generation also prevail, mainly by debating on either kinetic or potential energy (i.e., barotropic or baroclinic instability) is the main source of energy input (Constantinou & Hogg, 2019; Spall, 2000). Containing complex and nonlinear physics, mesoscale eddies have a spatial scale of  $\sim 100 \text{ km}$  and a growth period of about one month. According to these arguments on eddy dynamics, such nearly geostrophic vortical structures of the upper ocean are doubtlessly important in the redistribution of sea water properties and biogeochemical tracers across ocean basins (Dufour et al., 2015; Wunsch, 1999; Zhang et al., 2014).

Besides horizontal movement in the mechanical context, mesoscale eddies can also stamp prints on air-sea interactions, primarily by displaying sea surface temperature (SST) anomalies that modulate the thermal stability of marine atmospheric boundary layer (MABL) (Frenger et al., 2013; Villas Bôas et al., 2015; Song et al., 2016; Liu et al., 2020; Moreton et al., 2021), or representing a velocity anomaly compared to the sea surface current pattern that modifies the mechanical feedback to the atmosphere (Byrne et al., 2016; Rai et al., 2021). In terms of air-sea heat exchanges, anticyclonic eddies detected as positive sea surface height anomalies (SSHAs) typically tend to enclose a distinct warm temperature anomaly and thus warm the MABL. Cyclones, conversely, cool the MABL. This coherence between SST and SSH eddy contours is ascribed to the bending of isotherms in the ocean interior,

which is also exposed at sea surface as the dynamic topography. However, recent statistics have shown that about 20% of eddies detected from altimeter data exhibit unconventional characteristics, such as warm-core cyclones and cold-core anticyclones (Itoh & Yasuda, 2010; Moschos et al., 2022; Ni et al., 2021; Sun et al., 2022), which do not conform to the standard definition of eddies based on sea surface height and temperature coherence. We refer these atypical eddies as SSH-SST incoherent eddies hereafter. Generations of such counter-intuitive features at the mesoscale remain to be studied. In previous studies, eddies that are dynamically defined from altimeters have been separated based on either a performance of trapping water masses, or a functioning of stirring water properties in the vicinity [for example, in Frenger et al. (2018) and Dawson et al. (2018) that illustrate eddies' role in trapping or mixing chlorophyll].

While abundant evidence has discussed upon the mesoscale impact on sea surface properties [for example, studies on eddy-induced SST (Hausmann & Czaja, 2012), salinity (Melnichenko et al., 2017) and mixed layer depth (Gaube et al., 2019)], there is still a lack of knowledge on the potential contributions of the mechanically-defined mesoscale eddies on air-sea turbulent heat exchanges and their possible influence on the global heat budget. The present study aims to investigate the role of eddies in the latent heat flux (LHF) and sensible heat flux (SHF) in the North Indian Ocean basin, by merging two newly-developed remotely-sensed datasets: (a) the second generation of satellite-derived air-sea flux analysis on  $0.25^\circ \times 0.25^\circ$  resolution produced by the Objectively Analyzed Air-Sea Fluxes project [hereafter referred to as OAFflux2 (Yu, 2019)] that is able to resolve LHF, SHF and other air-sea properties at the corresponding scale (Liu et al., 2020), and (b) the Mesoscale Eddy Trajectories Atlas (META3.2 DT) derived from altimetric absolute dynamic topography (ADT) (Pegliasco et al., 2022). The OAFflux2 air-sea turbulent heat fluxes (THFs) are calculated from empirical bulk flux parameterizations using surface meteorological variables derived from microwave radiometers, sounders, and scatterometers. The eddy detection is literally dynamic but encloses thermal status of the ocean interior [that is, subsurface eddying structures are often visible at the sea surface, which might be tied with concepts of mode waters or intra-thermocline eddies (Barceló-Llull et al., 2017; Chen et al., 2022; McGillicuddy, 2015)]. Recently, Assassi et al. (2016) defined a simple index to separate surface- and subsurface-intensified eddies, principally characterized by a maximum potential vorticity located within or below the surface mixed layer. Similarly, SSH-SST coherent and incoherent eddies are also distinguishable from each other underneath the sea surface (Sun et al., 2022).

Here, we focus on eddy-induced air-sea heat fluxes in the North Indian Ocean, as this region is unique in the world ocean in that the seasonally reversing monsoon winds alternate the ocean circulation on a semi-annual basis (Schott & McCreary, 2001). Although many studies were carried out to understand the seasonality of monsoon currents and their transports [for example, low salinity water has been transported to Arabian Sea (AS) from the Bay of Bengal (BoB) in summer (Zhu et al., 2022)], less attention has been given to the impact of mesoscale eddies on air-sea exchanges in this region. A significant difference between AS and BoB is the abundance of freshwater influx from the major Indian rivers and precipitation in BoB, which leads to the presence of highly saline stratification and thick barrier layers near surface (He et al., 2020; Seo et al., 2019; Thadathil et al., 2007). Other differences between AS and BoB include the appearance of saline subsurface eddies near the upwelling coast (L'Hégaret et al., 2016), and intra-basin variance of eddy generation in the Arabian Sea (Varna et al., 2023).

The objectives of this study are to (a) estimate the LHF and SHF anomalies induced by mesoscale eddies in the AS and BoB, (b) describe the spatial distribution of mesoscale heat flux variability in the region and investigate its coupling to the eddy-induced SST, and (c) understand the effects of SSH-SST coherent and incoherent eddies on THF and their seasonal modulations. The data and methods are introduced in Section 2. Section 3 presents results addressing the three aims, and Section 4 concludes and discusses implications for future research.

## 2. Data and Methods

### 2.1. Eddy Detection and Tracking

We use the META dataset as eddy atlas (Pegliasco et al., 2022), in which a novel SSH-based automatic identification algorithm was applied to determine and track eddies through spatially high-pass filtered SSH-closed contours (Chelton et al., 2011). The date of eddy occurrence, location, radius, and amplitude are contained within this dataset, but information regarding eddy contours is absent. The amplitude of the anticyclonic (cyclonic) eddy is defined as the absolute difference between the maximum (minimum) sea level anomaly (SLA) values within the eddy range and the average SLA value at the eddy's edge. In this study, the time period chosen

for constructing eddy statistics and their correlation with air-sea variables is between 1999 and 2018 (i.e., 20 years in total).

Following detection of eddies, the construction of eddy trajectories is established by comparing the position of eddy centers over time. In the META algorithm, for any eddy detected at day  $D_0$ , it then follows to find eddies at day  $D_1$  within a circle with  $D_0$  eddy core as the center and  $D_0$  eddy radius  $R$  (determined by latitude) as the circle radius. If no target eddy is detected at day  $D_1$ , the algorithm goes to day  $D_2$  and the searching radius increases to 1.33  $R$ . This search continues and ends with day  $D_4$ , where the eddy trajectory is considered to have terminated if no eddy is found. The eddy lifespan can then be defined as the day number between the first identification and termination.

## 2.2. Sea Surface Turbulent Heat Fluxes

The LHF, SHF and related surface meteorological variables are taken from OAFflux2, which is a new satellite-derived 0.25-degree gridded air-sea flux analysis (1988 to the present) developed under the auspices of NASA's Making Earth System Data Records for Use (MEaSUREs) program. The computation of LHF and SHF is based on the version 3.6 of the Coupled Ocean-Atmosphere Response Experiment (COARE) bulk algorithm (Fairall et al., 2003):

$$\begin{aligned} LHF &= \rho L_e c_e U (Q_s - Q_a), \\ SHF &= \rho c_p c_h U (T_s - T_a), \end{aligned} \quad (1)$$

where  $\rho$  is air density and  $L_e$  is the latent heat of vapourization and is a linear function of SST ( $T_s$  in the function).  $c_p$  is the specific heat capacity of air at constant pressure, and  $c_e$  and  $c_h$  are the stability- and height-dependent turbulent exchange coefficients for latent and sensible heat.  $T_a$  and  $Q_a$  are the air temperature and specific humidity at the reference height of 2 m above the sea surface.  $U$  is the wind speed at the reference height of 10 m. Specific humidity  $Q_s$  is the saturation humidity at  $T_s$ . These two bulk formulas have linked LHF (SHF) to SST, wind speed and air-sea humidity difference (temperature difference). In OAFflux2,  $U$  is synthesized from 18 satellite sensors including both microwave radiometers and scatterometers (Yu & Jin, 2014a, 2014b), and  $Q_a$  and  $T_a$  are retrieved from 13 satellite microwave sounders and radiometers (Yu & Jin, 2018). Here, it is evident that both latent and sensible fluxes are functions of wind speed and temperature (referred to as the dynamic and thermodynamic factors hereafter).

## 2.3. Connection Between Fluxes and Eddies

Mesoscale eddies have typical horizontal scales of 50–300 km and time scales ranging from weeks to months. However, air-sea fluxes vary over a broad range of spatiotemporal scales. In order to isolate mesoscale features in the THF signal, each surface variable from the OAFflux dataset is filtered in both time and space. Following previous studies (Villas Bôas et al., 2015; Liu et al., 2018), a temporal band-pass Butterworth window is applied to preserve periods between 7 and 90 days, which correspond to the typical mesoscale in time. In the next step, a moving average Hann window is used to filter spatial scales larger than 600 km. Thus, these spatially-filtered maps containing signals with wavelengths longer than 600 km are taken as the large-scale reference level, which is then subtracted from the time-filtered maps to construct the anomaly maps associated with mesoscale features.

The spatial pattern of heat flux anomalies inside eddies and their immediate surroundings are estimated using composite maps. For each identified eddy, the anomalies are interpolated onto a uniform high-resolution grid, normalized by the radial distance from the eddy center to the eddy edge. The spatial extent of the grid is chosen to represent the anomaly fields to a distance twice the eddy radius  $R$  in each direction. This scaling allows one to average the anomaly of thousands of eddies as a single composite map, consisting of an efficient way to depict their mean signature on surface variables. The composite maps of eddy-induced anomalies are produced by averaging anomaly fields over all eddies selected by eddy types (Section 3.2) and time of year (Section 3.3). In this study, we separate warm and cold eddies in terms of extreme SST anomalies inside the eddy radius  $R$ . Warm-core eddies are determined if the extreme SST anomaly inside the eddy contour is positive. Similarly, a negative SST extremum inside the eddy contour defines a cold-core eddy. These two separations according to polarity and

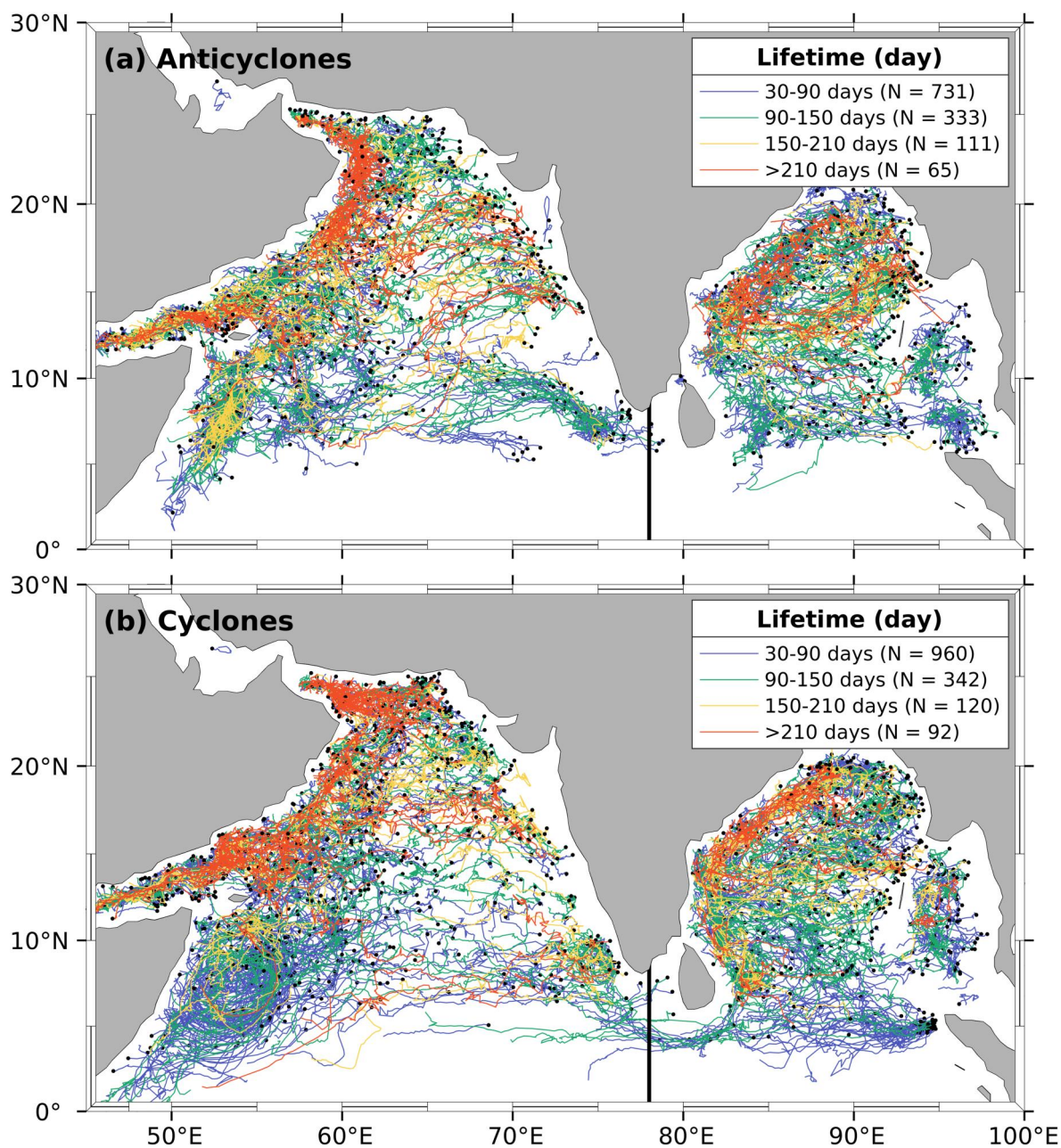


**Figure 1.** Trajectories of mesoscale eddies in the North Indian Ocean for the period of 1999–2018: (a) anticyclones; (b) cyclones. In each panel, eddy trajectories are divided into 4 classes in terms of their lifetime in days.  $N$  indicates the number of trajectories in each class. Eddies shorter than 30 days were excluded for analysis in this study.

temperature lead to four eddy types: SSH-SST coherent eddies (warm-AEs and cold-CEs), and SSH-SST incoherent eddies (warm-CEs and cold-AEs).

### 3. Results

#### 3.1. Eddy Characteristics in the North Indian Ocean

For the 20-year period (1999–2018), anticyclonic and cyclonic eddy trajectories (Figure 1) are frequently observed north of  $5^\circ$ , particularly near the western boundary currents of both the Arabian Sea (Somali Current and East Arabian Current) and the Bay of Bengal (East Indian Coastal Current). A schematic of Indian Ocean currents

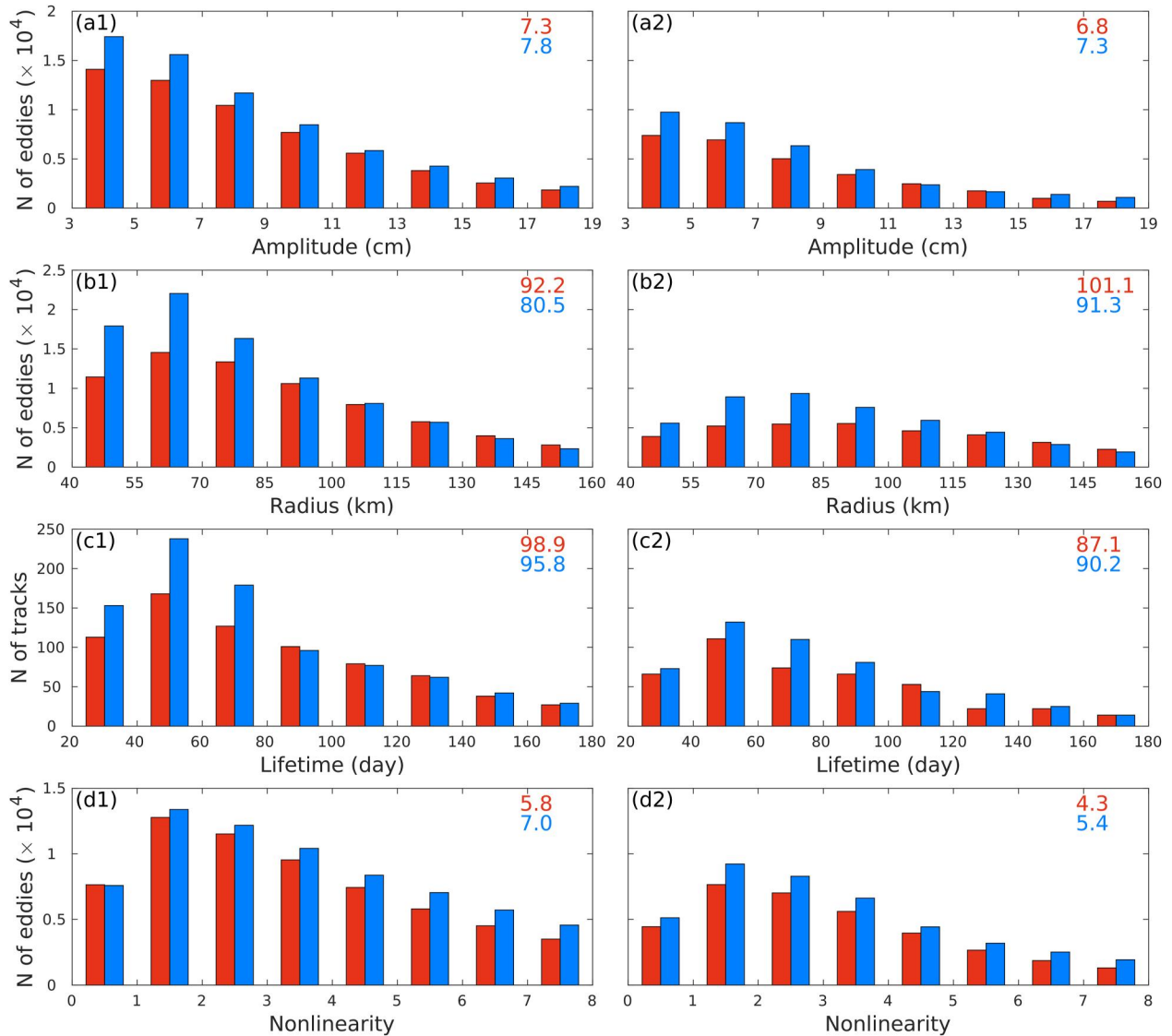


**Figure 2.** Eddy characteristics for (left) the Arabian Sea (AS) and (right) the Bay of Bengal (BoB): (a1) and (a2) eddy numbers as a function of eddy amplitude. (b1) and (b2) Eddy numbers according to the eddy radius. (c1) and (c2) Number of eddy tracks in terms of lifetime. (d1) and (d2) Eddy numbers as a function of nonlinearity (as defined in the text). Mean values for AEs (in red) and CEs (in blue) are displayed on the top right corner of each panel.

can be found in, for example, Phillips et al. (2021) Figure 10 for comparison. Eddies with a duration shorter than 30 days were excluded, which led to 1240 AE and 1514 CE trajectories. The locations of the longest trajectories are analogous to locations of the largest eddy amplitudes (not shown), measured as the ADT difference between the eddy center and its periphery. Though most eddies migrate westward due to  $\beta$ -effect, there are respectively 13% and 12% of AEs and CEs moving eastward.

Major statistical characteristics of eddies in the AS and BoB are shown in Figure 2. One notable feature is that the number of AEs (red color) is generally fewer than that of CEs (blue color) for all amplitudes, radii and lifespans in both AS (left panels) and BoB (right panels). In the AS, the average amplitudes vary from 3 to 11 cm, which account for 76.6% (77.6%) of AEs (CEs). For each polarity in the BoB, the average amplitudes of AEs (CEs) in the same range occupy 79.4% (81.5%). Typical values of the observed radius are between 40 and 115 km, with the largest group of eddies having a radius of 55–70 km in AS, and 70–85 km in the BoB.

In the AS, approximately 60.8% (55.4%) of AEs (CEs) last longer than 60 days, and about 29.0% (24.0%) AEs (CEs) have lifespan longer than 100 days. Contrastively, eddy lifetime is slightly shorter in the BoB, with 58.6%

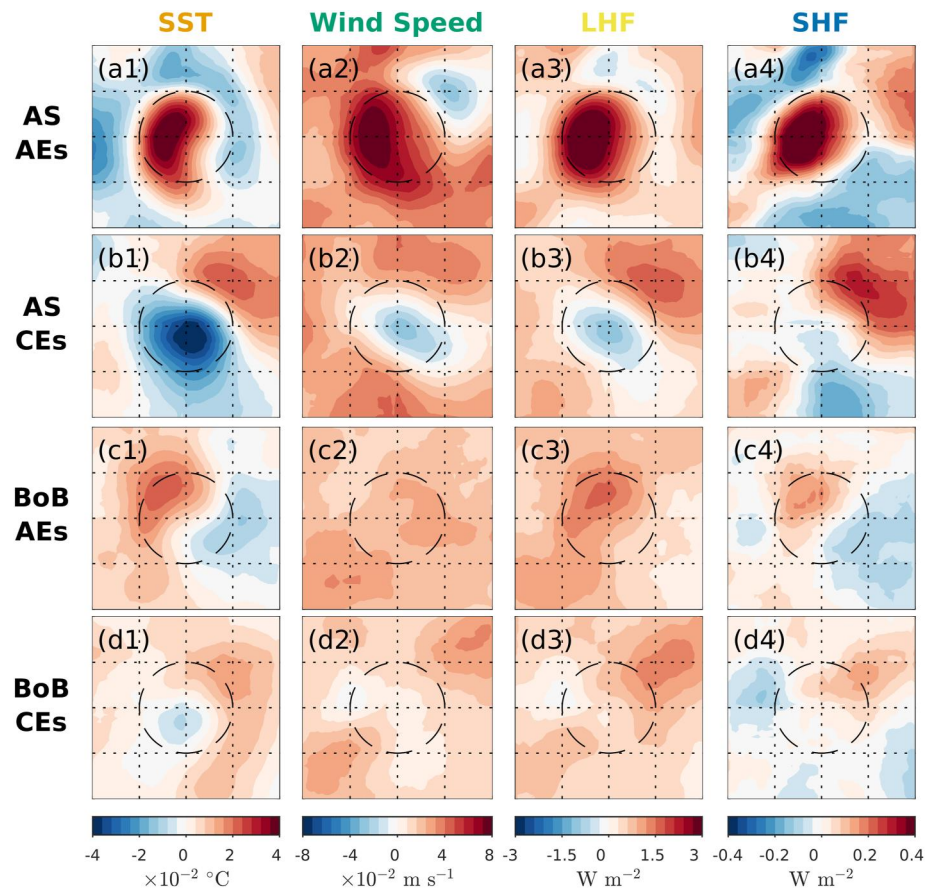


**Figure 3.** Composite maps of air-sea variables. From top to bottom, each row is associated with the Arabian Sea anticyclones (AEs), cyclones (CEs), the Bay of Bengal AEs and CEs. From left to right, each column displays sea surface temperature (SST), wind speed, latent heat flux (LHF) and sensible heat flux (SHF) anomalies. The axes in the composite maps are the normalized distance between the eddy center and twice the eddy edge. The circle of dashed lines in each map marks an eddy contour with the effective eddy radius.

(60.6%) and 25.9% (23.9%) surviving more than 60 and 100 days respectively. The bottom panels of Figure 2 display a measure of eddy nonlinearity, which is characterized by the ratio of the rotational speed  $U$  to the translation speed  $c$  of the feature. Note that the latter was computed from the migration of eddies (as the distance in eddy trajectories) divided by the time span. When this parameter is large, the eddy is prone to be nonlinear, which allows it to maintain a coherent structure as it propagates. In the AS, AEs (CEs) with a nonlinearity larger than 4 account for 33.9% (37.1%), while these percentages reduce to 28.4% (29.2%) in the BoB. That is to say, eddies in the AS tend to trap more water masses along their paths of migration compared with eddies in the BoB. In a nutshell, mesoscale eddies in the AS are smaller in space, thicker in surface displacement, longer in lifespan and more nonlinear in 3D shape compared with eddies in the BoB.

### 3.2. Signatures of SSH-SST Coherent and Incoherent Eddies on Heat Fluxes

Composite maps of air-sea variable anomalies for cyclonic and anticyclonic eddies will be explained in this section. Here, it has to be noted that we refer to mesoscale eddies detected from satellite altimetry as dynamic phenomena, while the air-sea variables such as SST and heat flux anomalies associated with eddies are their thermodynamic features.

The averaged spatial distribution of SST, wind speed, LHF and SHF anomalies inside eddies is shown in Figure 3. These composite maps were obtained by averaging eddy-induced anomalies of each variable with radius larger than 30 km and amplitude larger than 35 mm, corresponding to 79,440 anticyclonic and 93,643 cyclonic eddy realizations in the AS. The same selection in the BoB led to 39,195 anticyclones and 50,442 cyclones. The

**Table 1**  
*Eddy-Induced Air-Sea Variables for the Arabian Sea and Bay of Bengal*

Region Eddy types	Arabian Sea				Bay of Bengal			
	Warm-AEs (50.1%)	Cold-AEs (34.6%)	Cold-CEs (44.0%)	Warm-CEs (39.8%)	Warm-AEs (50.7%)	Cold-AEs (44.4%)	Cold-CEs (46.0%)	Warm-CEs (49.3%)
SST	0.32 ± 0.19	-0.31 ± 0.19	-0.32 ± 0.22	0.27 ± 0.16	0.25 ± 0.15	-0.27 ± 0.17	-0.26 ± 0.16	0.25 ± 0.15
Ts-Ta	0.33 ± 0.17	-0.31 ± 0.29	-0.29 ± 0.25	0.31 ± 0.16	0.30 ± 0.16	-0.31 ± 0.17	-0.30 ± 0.17	0.31 ± 0.16
Qs-Qa	0.47 ± 0.25	-0.43 ± 0.31	-0.42 ± 0.30	0.43 ± 0.25	0.45 ± 0.23	-0.42 ± 0.26	-0.41 ± 0.26	0.46 ± 0.24
WS	0.41 ± 0.36	-0.31 ± 0.36	-0.41 ± 0.41	0.36 ± 0.36	0.40 ± 0.33	-0.34 ± 0.28	-0.36 ± 0.32	0.39 ± 0.35
SHF	4.2 ± 3.2	-3.9 ± 3.9	-3.7 ± 3.5	3.6 ± 2.7	3.6 ± 2.7	-3.6 ± 2.6	-3.4 ± 2.6	3.7 ± 2.8
LHF	19.2 ± 14.4	-14.9 ± 12.0	-16.3 ± 12.8	16.3 ± 13.5	17.0 ± 11.6	-14.5 ± 9.8	-14.6 ± 10.1	17.0 ± 12.2
THF	22.7 ± 17.0	-18.0 ± 14.8	-19.2 ± 15.3	19.3 ± 15.4	20.0 ± 13.7	-17.4 ± 11.9	-17.4 ± 12.0	20.0 ± 14.3

*Note.* For each variable, the values displayed for warm-AEs and warm-CEs are maxima, while those shown for cold-AEs and cold-CEs are minima (i.e., extrema for these four eddy types). The percentages were calculated in terms of the same polarity and in the same region.

histogram of Figure 2 shows that cyclonic eddies are more than their anticyclonic counterparts, in terms of different amplitudes, radii and other eddy characteristics. Nonetheless, the dominant eddy-induced SST and heat flux anomalies (as to add AEs and CE together) display net positive values as shown in Figure 3 and Table 1. The comparison of SST anomalies between AS and BoB indicates that eddies in the AS tend to trap a warm/cold monopole of SST anomaly that is consistent with the eddy rotation, as shown in Figures 3a1 and 3b1. In other words, SSH-SST coherent eddies dominate in this region, albeit a small distance between the SST- and SSH-determined centers. This shift of SST anomaly from the SSH-based eddy core is mainly westward for AEs and southward for CE. In contrast to eddies in the AS, Figures 3c1 and 3d1 indicate that SST anomalies in the BoB are rather stirred by the whirling of eddies. A similar comparison between the AS and BoB for eddy-induced SST can also be obtained for the wind speed field, where eddy-induced anomalies of both polarities in the BoB display a slightly positive anomalous value [in Figures 3c2 and 3d2].

Similar to SST and wind speed composites (Figure 3), we also note that the extreme anomalies of LHF and SHF in the averaged composite maps do not coincide with the eddy centers but are slightly skewed for the AS eddies and largely displaced for the BoB eddies. In the AS, the extreme LHF (SHF) anomalies near the eddy centers reach  $3.8 \text{ W m}^{-2}$  ( $0.5 \text{ W m}^{-2}$ ) for AEs and  $-1.1 \text{ W m}^{-2}$  ( $-0.2 \text{ W m}^{-2}$ ) for CE respectively. These values are smaller in the BoB: the maximum LHF (SHF) anomaly for AEs is  $1.7 \text{ W m}^{-2}$  ( $0.2 \text{ W m}^{-2}$ ) inside the eddy contour, and the minimum for CE is  $-0.2 \text{ W m}^{-2}$  ( $-0.1 \text{ W m}^{-2}$ ). Note that these values are extremes of each composite map in a statistical context, which are incompatible with extremes of each eddy. Components of LHF and SHF (i.e., air-sea humidity and temperature differences,  $Q_s - Q_a$  and  $T_s - T_a$ ) display almost identical patterns to LHF and SHF, and thus are neglected for a duplicate of plotting. This consistency between heat fluxes (LHF and SHF) and their components ( $Q_s - Q_a$  and  $T_s - T_a$ ) suggests a dominance of thermal factors in the mesoscale air-sea heat exchange.

In order to obtain a relationship between eddy-induced SST and THF, Figures 4 and 5 show composite maps of LHF, SHF, and SST divided into four components: warm-AEs, cold-AEs, cold-CEs and warm-CEs. This division allows us to infer (a) the proportion of SSH-SST incoherent eddies (i.e., cold-AEs and warm-CEs) in all eddies; (b) how these eddies differ from SSH-SST coherent eddies in shaping heat fluxes; and (c) the combination of SSH-SST coherent/incoherent eddies in forming an ensemble picture of eddy-induced THF. Besides LHF and SHF, Table 1 summarizes all air-sea variable anomalies in terms of these four eddy types.

In the AS, warm-AEs and cold-CEs respectively take up 50.1% of all AEs and 44.0% of all CE, while cold-AEs and warm-CEs occupy 34.6% and 39.8%. Note that some proportion of eddies is undetermined in terms of their SST anomalies, which is in part due to a vague comparison between positive and negative SST extrema inside eddy contours. Nonetheless, it is remarkable that SSH-SST incoherent eddies are prevailing in the region. A similar conclusion can be drawn for the BoB that the number of SSH-SST incoherent eddies is on the same order of coherent eddies.

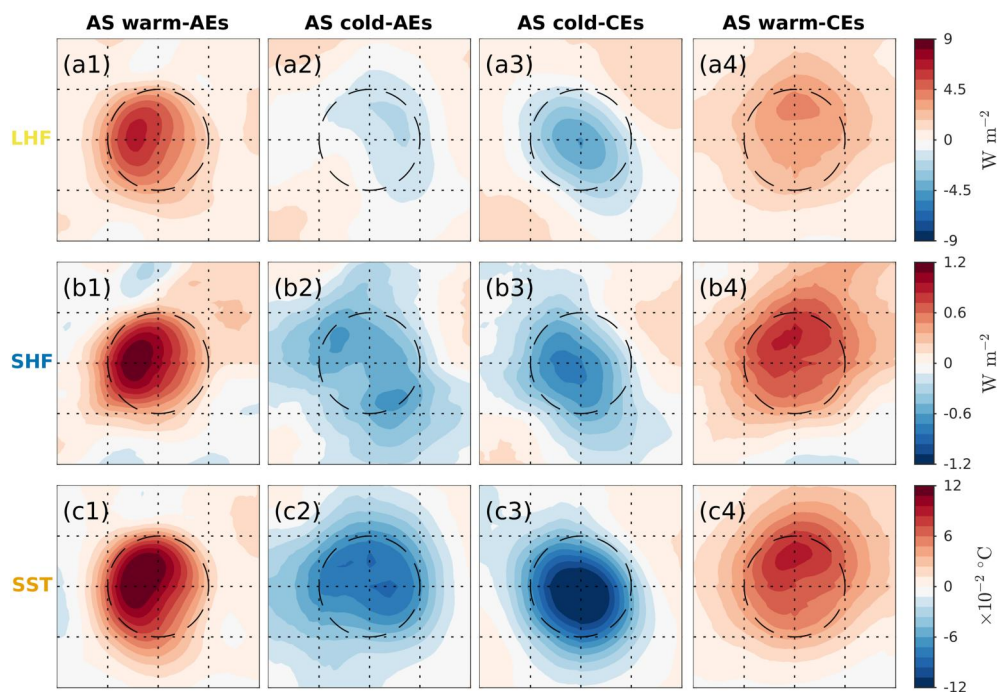


**Figure 4.** Composite maps of sea surface temperature (SST) and heat fluxes in the Arabian Sea. Panels (a1)–(a4) display latent heat flux (LHF) associated with warm-AEs, cold-AEs, cold-CEs, and warm-CEs. The following rows (b1)–(b4) and (c1)–(c4) show sensible heat flux (SHF) and SST.

Despite a similar quantity of eddies, the combination of Figures 4c1 or 4c2 and 3a1 indicates that warm-AEs in the AS are associated with a more concentrated warm anomaly compared with a relatively smaller magnitude of cold anomaly for cold-AEs. This explains the ultimate monopolar warm-core pattern for all AEs in a compositing census. For the AS CEs, a comparison between Figures 4c3 or 4c4 and 3b1 tells the same story. A recent study of

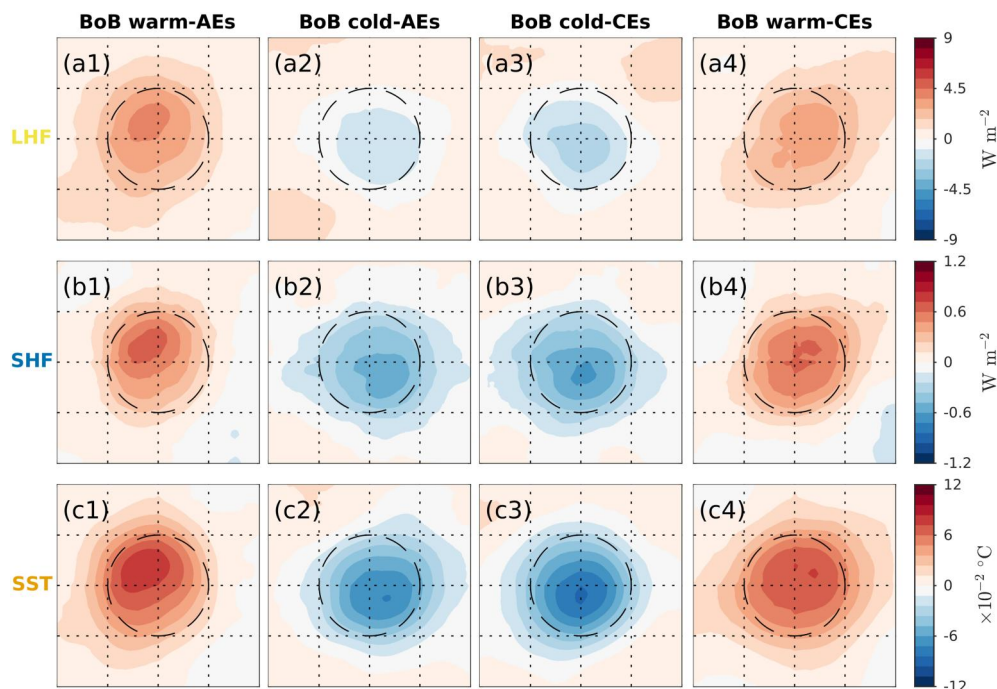


**Figure 5.** Same as Figure 4 but for the Bay of Bengal.

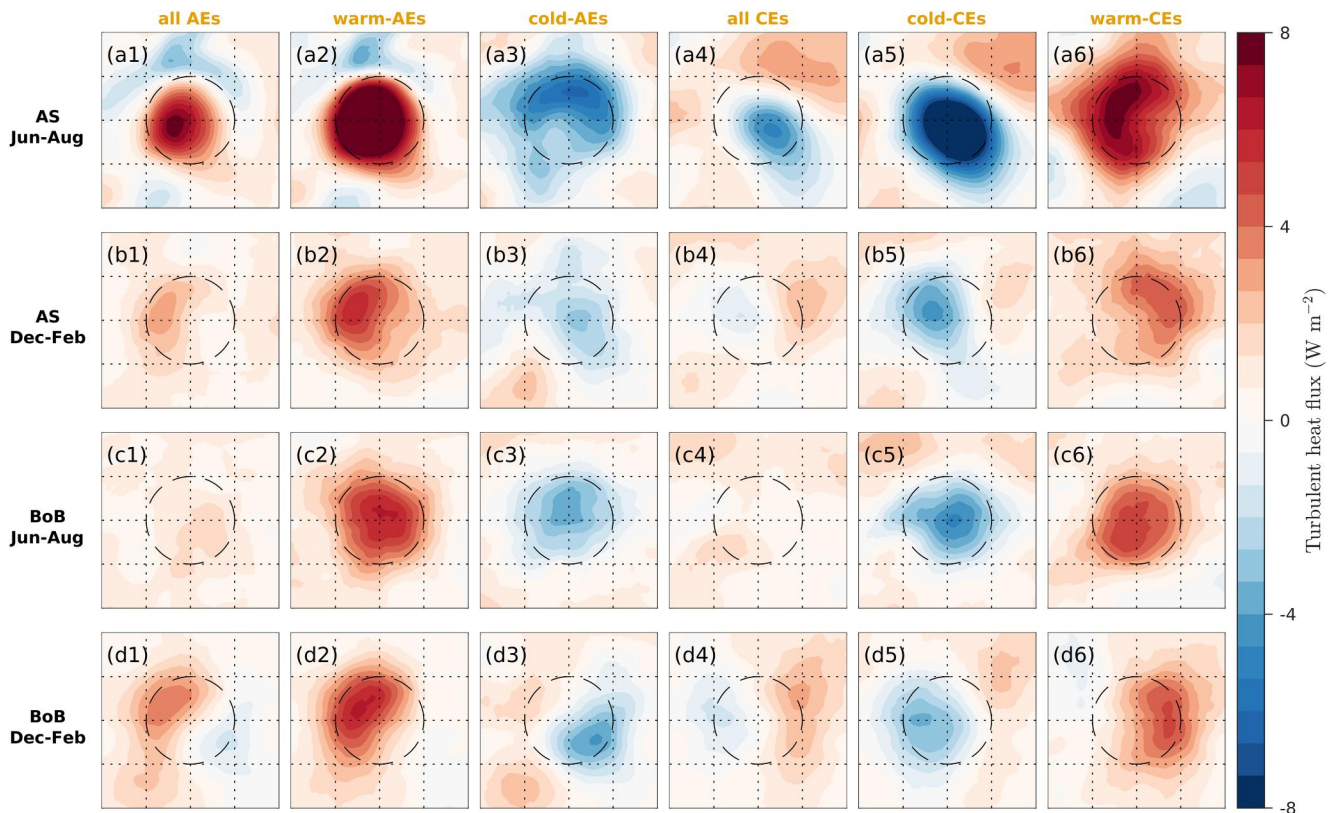


**Figure 6.** Turbulent heat fluxes (THFs) associated with SSH-SST coherent and incoherent eddies. Panels (a1)–(a6) display THF of the Arabian Sea in the summer monsoon season (June–August) in terms of all AEs, warm-AEs, cold-AEs, all CEs, cold-CEs, and warm-CEs. The second row (b1)–(b6) shows winter (December–February) THF in the Arabian Sea. Rows (c1)–(c6) and (d1)–(d6) display the same information for the Bay of Bengal.

Trott et al. (2019) also separated high-amplitude eddies in the AS based on both criteria of SSH and SST. Their results instead suggested that for both warm- and cold-core eddies in each polarity, the magnitudes of SST anomaly are approximately the same, while the SST centers are shifted in different directions. The inconsistency between our results and theirs might be in part due to a much larger amount of eddies in our study for the statistical analysis. In addition, the eddy detecting method is similar in both studies, while anomalies of air-sea variables are computed in different manners. In terms of the BoB, as shown in the bottom row of Figure 5, SST anomalies of these four eddy types are comparable, which can generate an averaged dipole pattern when combined together [Figures 3c1 and 3d1].

### 3.3. Seasonal Influence on Eddy-Induced SST-THF Coupling

In this section, further analysis on the seasonality of SST-THF coupling will be discussed. Summer and winter seasons are defined as 3-month periods from June to August, and from December to February separately. In Figure 6, such separation is presented by illustrating the total THF patterns of both SSH-SST coherent and incoherent eddies.

As discussed in Section 3.2, a typical SSH-THF coherent anticyclone originates from a combination of stronger warm-core AEs and weaker cold-core AEs. This combination is a consequence of either outnumbered warm-core AEs over cold-core AEs, or concentrated warm monopoles dominantly located at the eddy center. The first row of Figure 6 shows eddy-induced THF in the summer (June–August) of the Arabian Sea. Along with statistics in Table 2, warm-AEs outnumber cold-AEs by approximately 20% for constructing a positive monopolar pattern of THF located at the eddy center. This also applies to CEs in composing a net negative THF monopole as shown in (a4), with a slightly southeastward shift of the minimum flux as the core. In comparison to summer, the magnitude of winter-time (December–February) THF induced by eddies is much smaller, albeit maintaining a shifted monopole in contrast to the eddy contours.

**Table 2**  
*Seasonality of Turbulent Heat Fluxes in Both Basins*

	all AEs		warm-AEs		cold-AEs		all CEs		cold-CEs		warm-CEs	
AS Jun–Aug	20,841	7.9	52.5%	14.2	30.0%	−6.2	19,985	−4.9	50.7%	−11.5	33.9%	8.1
AS Dec–Feb	18,099	3.2	49.3%	5.9	33.3%	−3.0	24,263	−1.4	43.7%	−4.4	39.5%	4.7
BoB Jun–Aug	8,993	1.8	46.9%	6.1	43.3%	−3.8	12,261	−0.4	45.6%	−4.9	51.2%	5.3
BoB Dec–Feb	10,781	4.0	54.3%	6.3	43.3%	−4.1	12,673	−1.7	46.7%	−3.6	47.3%	4.9
AS Mar–May	24,305	2.9	51.6%	4.8	34.4%	−1.8	26,438	−0.5	40.3%	−2.6	42.2%	4.6
AS Sep–Nov	16,195	3.9	45.7%	7.2	42.0%	−3.0	22,957	−0.7	42.6%	−4.6	42.3%	4.1
BoB Mar–May	9,136	1.9	54.8%	3.7	42.3%	−1.5	12,433	−0.4	46.1%	−2.3	47.9%	3.2
BoB Sep–Nov	10,285	1.2	46.7%	3.9	48.3%	−2.3	13,075	0.1	45.8%	−2.9	50.9%	3.6

*Note.* Number of eddies is displayed for all AEs or CEs in the Arabian Sea (AS) and Bay of Bengal (BoB), while the percentage is shown for each type of eddies. Statistics of the upper 4 rows correspond to Figure 6, while the lower 4 rows are displayed for a thorough comparison with the other two seasons (namely March–May and September–November). The values listed are minima for cold-core eddies and maxima for warm-core eddies inside the eddy contours. Units for heat fluxes:  $\text{W m}^{-2}$ .

Different from the AS, for which seasons significantly determine the magnitude of total eddy-induced THF, the temporal variation of THF in BoB is smaller (Table 2). For both seasons, the effects of SSH-SST incoherent eddies (warm-CEs and cold-AEs) compensate those of SSH-SST coherent eddies (warm-AEs and cold-CEs). In summer, extreme THF anomalies of both SSH-SST coherent and incoherent eddies are located near the eddy center, with offsetting consequences that lead to  $1.8 \text{ W m}^2$  for all AEs and  $-0.4 \text{ W m}^2$  for all CEs. In winter, however, SSH-SST coherent and incoherent eddies induce oppositely-directed shifts of THF cores. For example, composites of warm-AEs and cold-AEs [as shown in Figures 6d2 and 6d3] are situated at the northwestern and southeastern boundaries of the eddy contour. The aggregate of these two patterns results in a dipole of the total signal in (d1). It is also the case for BoB CEs in winter, where cold-CEs generate a negative THF anomaly at west while warm ones induce a positive anomaly at east. For the other two seasons (March–May as spring and September–November as autumn), the monopolar signature is also visible in the Arabian Sea. However in the BoB, the spring THF composites indicate dipoles in both AEs and CEs, while the autumn structure is resulted from a compensation between SSH-SST coherent and incoherent eddies (not shown).

In brief, for both summer and winter seasons in the AS, monopolar structures of THF are evident when compositing all eddies with the same polarity together. This monopole has been widely acknowledged as the eddy-trapping effect. However in the BoB, summer-time THF indicates a cancellation between warm-core and cold-core eddies since both eddies are associated with concentrated THFs near the cores. However in winter, warm-core and cold-core eddies in the BoB generate THF anomalies that shift in opposite directions, which unite to be a dipole that has been attributed to the eddy-stirring effect. Seasonal influence on these different mechanisms identified as either trapping or stirring has been shown in precipitation (Liu et al., 2018) and chlorophyll (Dawson et al., 2018). However, none of previous studies on seasonal variations have separated mesoscale eddies based on SST anomalies and investigated the combination of warm and cold eddies in constructing temporal differences.

### 3.4. Dynamic and Thermodynamic Contributions to Eddy-Induced Air-Sea Coupling

To examine the dynamic and thermodynamic contributions to heat fluxes, Figure 7 shows the extreme values of LHF (SHF) anomalies in the averaged composite maps as a function of wind speed and air-sea humidity difference (temperature difference). Regardless of the eddy polarity and basin, the magnitude of LHF and SHF anomalies increases with wind speed and air-sea humidity or temperature difference. Such dependence is approximately linear at lower values of wind speed,  $Q_s - Q_a$  and  $T_s - T_a$  anomaly. As indicated in Figures 7a1 and 7b1, within the wind speed anomaly from  $-1$  to  $1$ , both slopes in terms of LHF-wind speed and SHF-wind speed coupling are slightly larger for the AS than for the BoB. This suggests that variations in the wind field at the corresponding scale in the North Indian Ocean (e.g., seasonal reversions of monsoon winds or wind direction alterations at the mesoscale) might impose a larger influence on the heat flux responses in the AS compared with BoB.

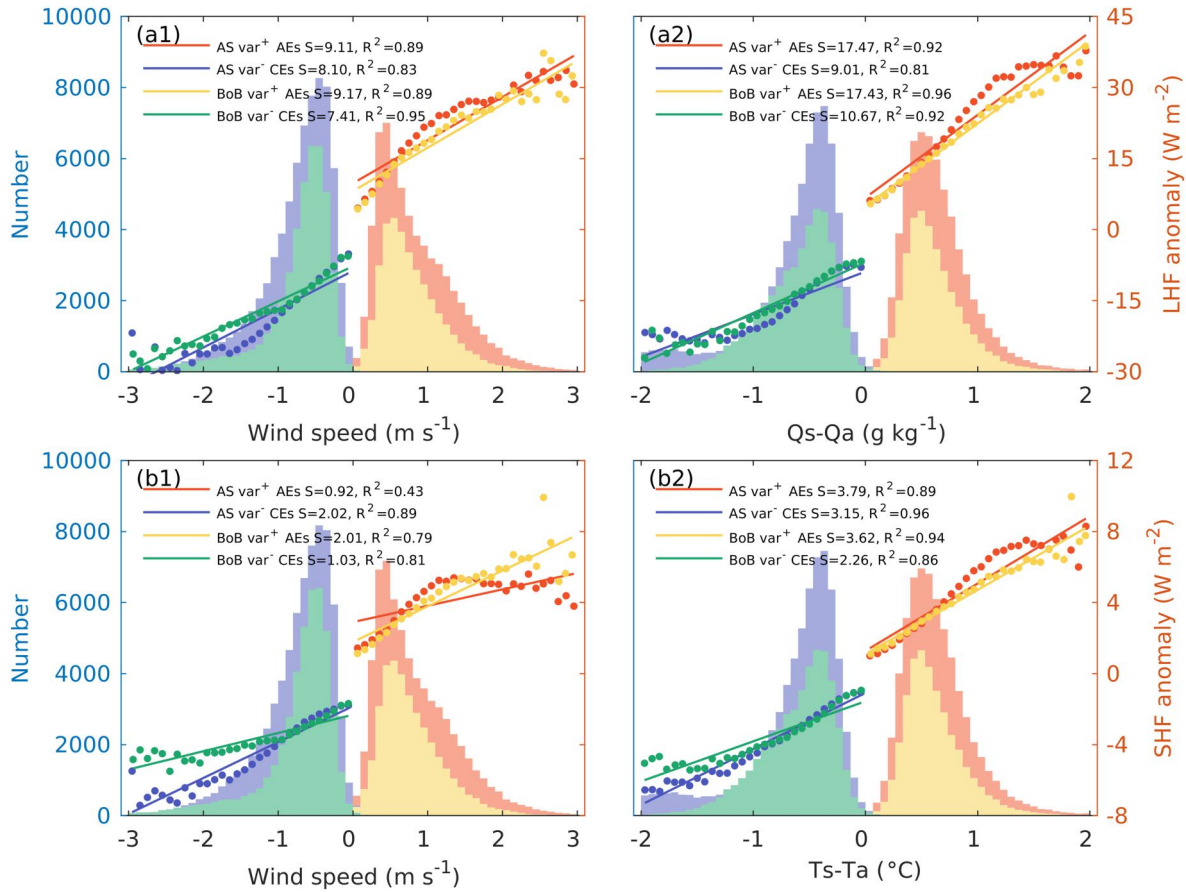


**Figure 7.** Relationship between heat fluxes and thermodynamic/dynamic factors in the bulk formula. Panels (a1) and (a2) show LHF anomaly as functions of wind speed and air-sea difference in specific humidity. (b1) and (b2) indicate SHF anomaly as functions of wind speed and air-sea difference in temperature. Bar plots at background indicate the number of eddies found in each bin of the  $x$ -axis. For each line,  $S$  is the coupling coefficient (slope of the linear regression) and  $R^2$  indicates the coefficient of determination.

Figure 8 and Table 3 show the coupling between eddy-induced SST and heat fluxes. For four eddy types in the two regions, both LHF and SHF anomalies are linearly related to SST anomalies within the temperature range between  $-1$  and  $1$  K (not shown). However as illustrated in the spatial distribution of SST-THF coefficients (Figure 8), though the largest amount of eddies for each type are found at the western boundaries (i.e., see the bottom two rows of Figure 8), it remains slightly unclear of an unambiguous spatial patterns for the eddy coefficients (i.e., the first two rows). In terms of coherent eddies, the coupling feedback coefficient of warm-AEs is slightly larger than cold-CEs, as displayed in Table 3. For the spatial distribution in the AS, warm-AEs are more likely to induce higher THF at the Gulf of Aden that interacts with the Somali Current, in the middle of AS basin, and at the inter-basin channel southwest of Sri Lanka. The BoB warm-AEs, however, may impose a uniformly large influence on the THF, with an intensity at the western boundary. In terms of SST-THF coupling associated with cold-CEs, higher THF is located at the eastern boundary of the Arabian Sea that connects the Gulf of Oman from the north and inter-basin region at the southern tip of India.

Figures 8a3 and 8b3 indicate the incoherent eddy signatures in SST-THF feedback. Interestingly for the AS, the spatial distribution of coefficients for cold-AEs is similar to that of cold-CEs, while an analogous comparison can be observed between warm-CEs and warm-AEs (with a larger amplitude for warm-CEs than warm-AEs). This larger amplitude of feedback [that is, compare (a2) with (b3)] suggests that warm-CEs release more heat than warm-AEs, especially at the middle of the basin and along the western boundaries. Overall, the impacts of incoherent eddies are not able to cancel those of coherent eddies in the Arabian Sea. An attempt of air-sea coupling between eddy amplitudes and THF anomalies also shows that incoherent eddies associated with higher absolute values of SSH-THF coefficients are distributed at similar regions to coherent eddies (not shown).

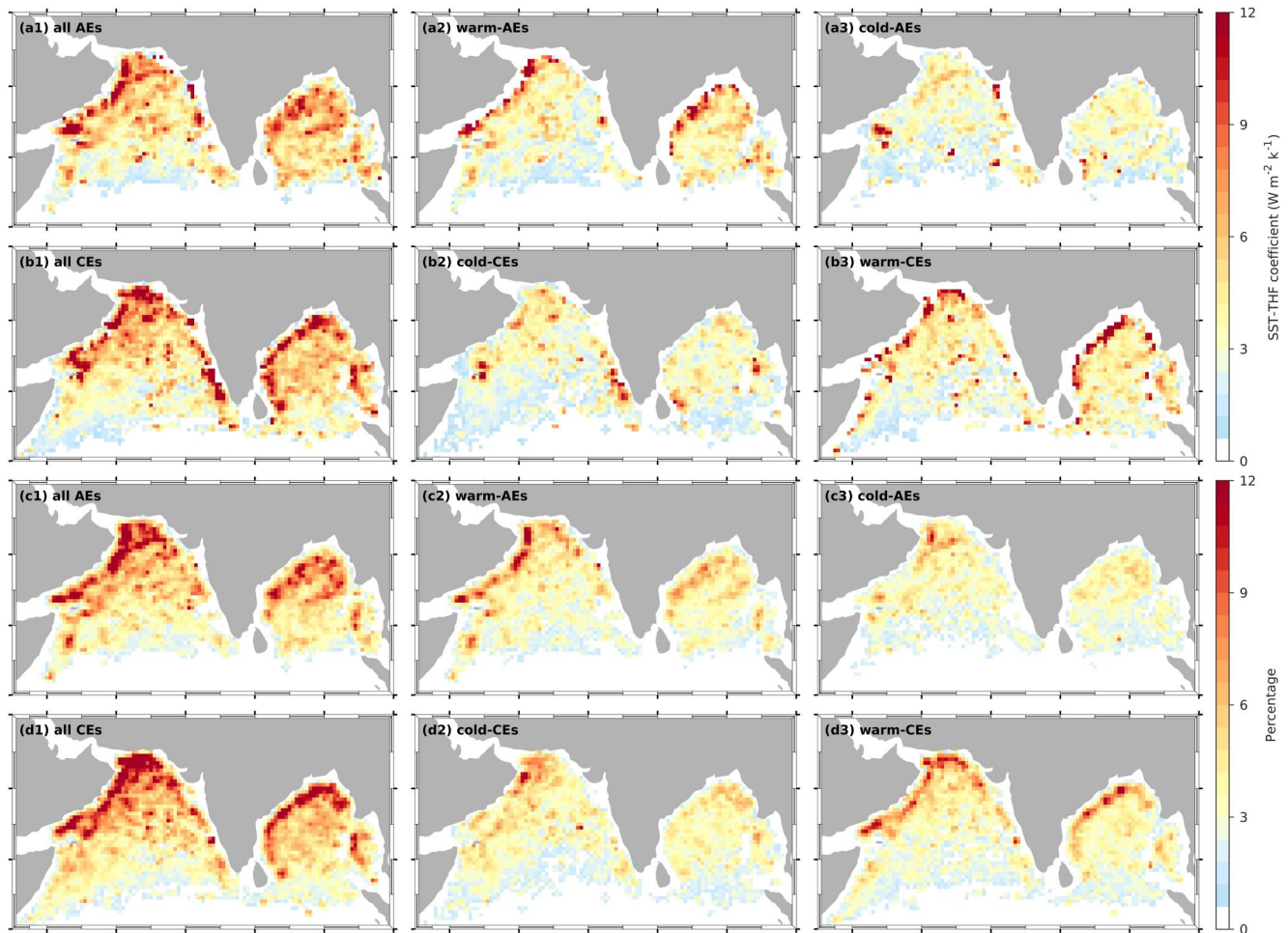


**Figure 8.** The coupling between SST and THF anomalies induced by eddies. Panels (a1)–(a3) show spatial maps of SST-THF coupling coefficient for all AEs, warm-AEs and cold-AEs. Panels (b1)–(b3) provide the same information for CEs. The values displayed are the median coefficients found in each  $0.5^\circ \times 0.5^\circ$  grid box. The last two rows display spatial distributions of eddy percentages in terms of days per year for each eddy type shown in the upper two rows.

Studies have shown that a larger warm eddy can thicken the atmospheric boundary layer which further leads to an amplified THF (Lin & Wang, 2021). Here, we notice that the cancellation between coherent and incoherent eddies in SSH-THF coupling at the basin scale does not reduce to zero.

#### 4. Summary and Discussions

For a 20-year combination of eddy detection and satellite-derived air-sea heat flux estimations, we have provided further evidence for the coupling between ocean and atmosphere at the mesoscale. In a conventional context, THF anomalies in the Indian Ocean associated with anticyclonic (cyclonic) eddies are positive (negative), implying an

**Table 3**  
*Eddy-Induced SST-THF Coupling Coefficients for the Arabian Sea and Bay of Bengal*

Region	Arabian sea				Bay of Bengal			
	Warm-AEs	Cold-AEs	Cold-CEs	Warm-CEs	Warm-AEs	Cold-AEs	Cold-CEs	Warm-CEs
LHF coef	31.4	16.8	21.8	23.2	26.2	22.0	21.4	25.3
SHF coef	7.6	5.9	5.7	5.4	5.4	5.1	4.5	5.0

*Note.* \*The coefficients were calculated within the SST anomaly range between  $-1$  and  $1$  k (i.e., within the linear relationship between SST and heat flux). *Note.* \*Units for coefficients:  $W\ m^{-2}\ k^{-1}$ .

increased (decreased) oceanic heat release with respect to a uniformly outgoing large scale turbulent flux. In this study, composite maps of SSH-SST coherent eddies (warm-AEs and cold-CEs) in the North Indian Ocean reveal a well-defined quasi-circular imprint within the eddy interior, with relatively strong turbulent heat flux anomalies near the center of the most energetic eddies ( $\sim\pm 21 \text{ W m}^{-2}$  for the Arabian Sea and  $\sim\pm 19 \text{ W m}^{-2}$  for the Bay of Bengal), decaying radially outward. On average, eddy-induced THF feedback for SSH-SST coherent eddies can approach  $\sim 40 \text{ W m}^{-2} \text{ K}^{-1}$  for warm-core AEs and  $\sim 28 \text{ W m}^{-2} \text{ K}^{-1}$  for cold-core CEs at its extreme value. In the North Indian Ocean, these mesoscale impacts on heat fluxes are much stronger than the large scale influence [for example, compared with Raj Parampil et al. (2016)].

However, maximum LHF and SHF anomalies are slightly shifted compared with the eddy contours defined by SSH (ADT to be more specific). Figure 9a displays a schematic of possible structures of coherent eddies in depth. Within the surface mixed layer defined by density (e.g., within  $\rho_1$  and  $\rho_2$  for AEs and  $\rho_4$  and  $\rho_5$  for CEs), sub-layers of temperature can be attained and exhibit a center shift in terms of the vertical. Such theory might explain the discrepancy between SST and SSH eddy centers. By co-locating Argo profiles with mesoscale eddies, Li et al. (2022) also found that coherent eddies in the global ocean are prevalently vertical tilted, with stratification and eddy size being key factors. Though absent in the text, the relationship between eddy's radius and flux anomalies was also investigated in this study. The intensity of THF anomalies in coherent eddies increases with the eddy radius, indicating that large eddies have a stronger impact on the surface turbulent heat fluxes than small eddies. However, the eddy amplitude does not always affect heat fluxes in the Bay of Bengal. Details of how an eddy's dynamic and thermodynamic features evolve along its trajectory of migration need further investigations.

In addition to conventional SSH-SST coherent eddies, our results suggest a considerable contribution from SSH-SST incoherent eddies to heat fluxes [for example, a possible vertical structure of incoherent eddies is displayed in Figure 9b]. This contribution is sometimes negligible to influences of coherent eddies (as in the Arabian Sea), in some cases offsetting the patterns developed by coherent eddies (as in the Bay of Bengal summer monsoonal season), or occasionally forming a dipolar structure combined with coherent eddies (as in the Bay of Bengal winter). For both incoherent AEs and CEs, we propose in Figure 9b that subsurface features play a crucial role in shaping the surface SSH signals that mechanically define polarities of eddies. A previous study of Chaigneau et al. (2011) summarized that for the South Pacific Ocean, the core of CEs is located above the core of AEs due to different mechanisms of eddy formation. Therefore, these incoherent eddies should be taken into account in constructing numerical models to allow for a better understanding and representation of the processes governing the upper ocean heat budgets.

The question we have not tackled here is the distance between SST/THF centers and the SSH-based eddy cores. Several studies attribute this distance to air-sea heat exchanges along eddy migrations. That is to say, the heat or freshwater exchanges between mesoscale eddies and the overlying atmosphere could impact the eddy decay rate and lifetime. The signature of a recently formed eddy on the SST could be progressively eroded by surface heat fluxes, which gradually decrease the air-sea temperature gradients. Thus, stronger SST and THF anomalies are preferentially observed in regions of eddy genesis. On the other hand, extreme synoptic events passing over might be of interest for an interplay between the formation of mesoscale eddies and air-sea coupling. Also not discussed here are (a) the conditions for the occurrence of the SST-SSH incoherent eddies, (b) the mesoscale circulation patterns associated with these two classes of eddies and their impacts on the shift of SST core from SSH, and (c) impacts of the cancellation between coherent and incoherent eddies on air-sea feedback for the basin scales.

Another theory assigns the shift of eddy-induced SST/THF cores to mechanisms below the mixed layer, and thus eddies are separated based on the vertical location of potential vorticity (i.e., vertical gradient of potential density as the first order). For example, surface-intensified anticyclonic eddies have the largest deformation of isopycnals at the surface while those intensified at the subsurface are domed above the center and depressed below it. Likewise, subsurface-intensified cyclones have a depressed isopycnal shape above and a domed shape below (Assassi et al., 2016). In a nutshell, further investigations on the evolution of such anomalies following individual eddies are needed in order to better understand how the air-sea heat fluxes change during the eddy life cycles and how they affect the eddy decay rate. In addition, coupled climate models should be capable of representing air-sea interactions at mesoscales to enhance the accuracy of their predictions.

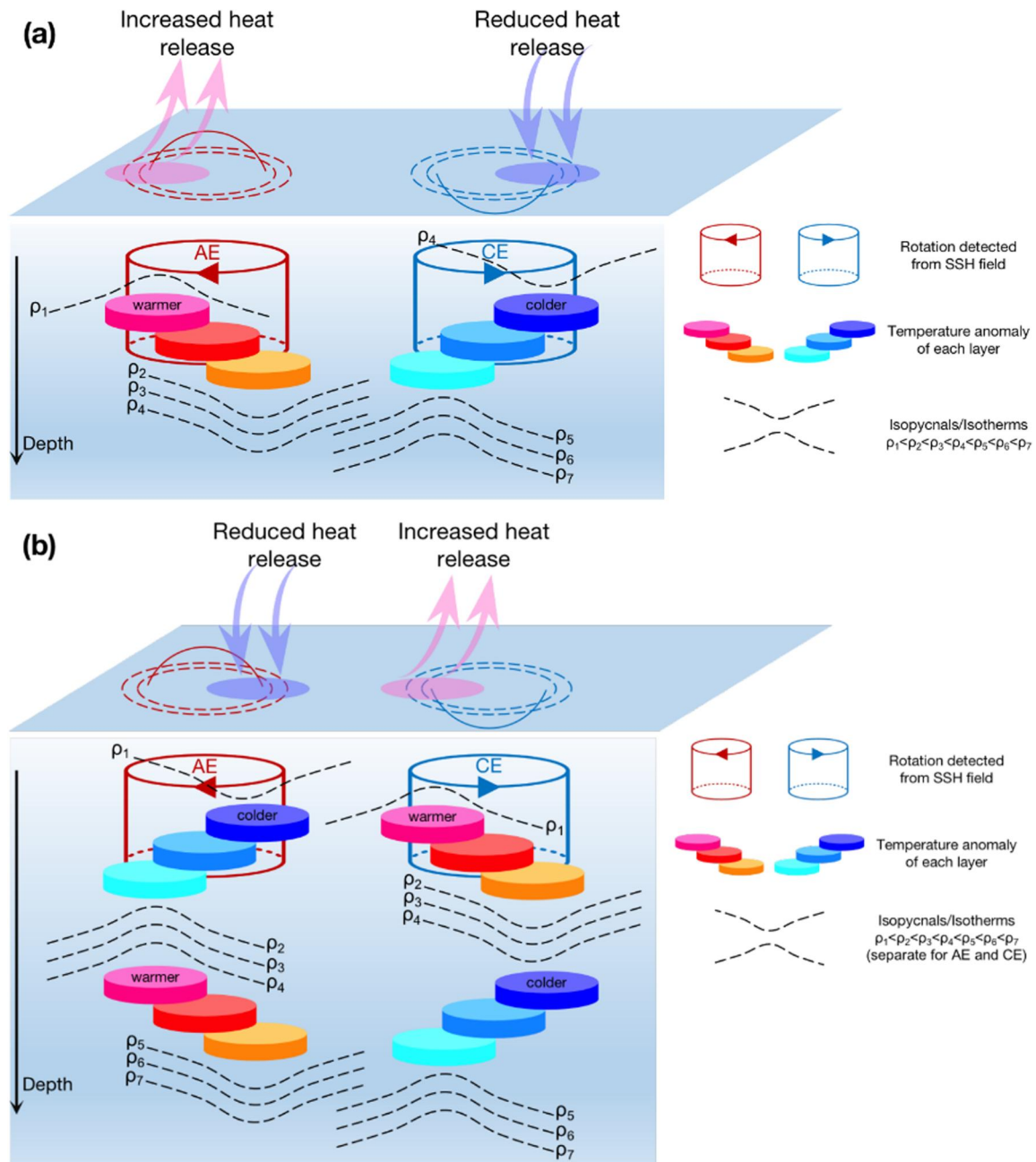


**Figure 9.** Schematic of anticyclonic and cyclonic eddies in depth. Panel (a) illustrates an example of SSH-SST coherent eddies, and (b) shows a possible vertical structure of SSH-SST incoherent eddies.

### Data Availability Statement

The high-resolution heat fluxes provided by the WHOI OaFlux project (Yu, 2019) are available at <https://oafux.who.edu/data-access/>. The META eddy atlas provided by AVISO (Pegliasco et al., 2022) is available at <https://www.aviso.altimetry.fr/en/data/products/value-added-products/global-mesoscale-eddy-trajectory-product/meta3-2-dt.html>.

**Acknowledgments**

We thank the reviewers for offering comments that led to improvements of the manuscript, and we gratefully acknowledge support from NOAA Ocean Monitoring and Observing (GOMO) program, Grant NA19OAR4320074.

**References**

Abernathey, R., & Cessi, P. (2014). Topographic enhancement of eddy efficiency in baroclinic equilibration. *Journal of Physical Oceanography*, 44(8), 2107–2126. <https://doi.org/10.1175/JPO-D-14-0014.1>

Assassi, C., Morel, Y., Vandermeirsch, F., Chaigneau, A., Pegliasco, C., Morrow, R., et al. (2016). An index to distinguish surface- and subsurface-intensified vortices from surface observations. *Journal of Physical Oceanography*, 46(8), 2529–2552. <https://doi.org/10.1175/JPO-D-15-0122.1>

Barceló-Llull, B., Sangrà, P., Pallàs-Sanz, E., Barton, E. D., Estrada-Allis, S. N., Martínez-Marrero, A., et al. (2017). Anatomy of a subtropical intrathermocline eddy. *Deep Sea Research Part I: Oceanographic Research Papers*, 124, 126–139. <https://doi.org/10.1016/j.dsr.2017.03.012>

Barthel, A., Hogg, A. M., Waterman, S., & Keating, S. (2022). Baroclinic control of southern ocean eddy upwelling near topography. *Geophysical Research Letters*, 49(7), e2021GL097491. <https://doi.org/10.1029/2021GL097491>

Byrne, D., Münnich, M., Frenger, I., & Gruber, N. (2016). Mesoscale atmosphere ocean coupling enhances the transfer of wind energy into the ocean. *Nature Communications*, 7(1), ncomms11867. <https://doi.org/10.1038/ncomms11867>

Chaigneau, A., Le Texier, M., Eldin, G., Grados, C., & Pizarro, O. (2011). Vertical structure of mesoscale eddies in the eastern South Pacific Ocean: A composite analysis from altimetry and Argo profiling floats. *Journal of Geophysical Research*, 116(C11). <https://doi.org/10.1029/2011JC007134>

Chelton, D. B., Schlax, M. G., & Samelson, R. M. (2011). Global observations of nonlinear mesoscale eddies. *Progress in Oceanography*, 91(2), 167–216. <https://doi.org/10.1016/j.pocean.2011.01.002>

Chen, Y., Speich, S., & Laxenaire, R. (2022). Formation and transport of the south Atlantic subtropical mode water in eddy-permitting observations. *Journal of Geophysical Research: Oceans*, 127(1), e2021JC017767. <https://doi.org/10.1029/2021JC017767>

Constantinou, N. C., & Hogg, A. M. (2019). Eddy saturation of the southern ocean: A baroclinic versus barotropic perspective. *Geophysical Research Letters*, 46(21), 12202–12212. <https://doi.org/10.1029/2019GL084117>

Dawson, H. R. S., Strutton, P. G., & Gaube, P. (2018). The unusual surface chlorophyll signatures of southern ocean eddies. *Journal of Geophysical Research: Oceans*, 123(9), 6053–6069. <https://doi.org/10.1029/2017JC013628>

Dufour, C. O., Griffies, S. M., de Souza, G. F., Frenger, I., Morrison, A. K., Palter, J. B., et al. (2015). Role of mesoscale eddies in cross-frontal transport of heat and biogeochemical tracers in the southern ocean. *Journal of Physical Oceanography*, 45(12), 3057–3081. <https://doi.org/10.1175/JPO-D-14-0240.1>

Fairall, C. W., Bradley, E. F., Hare, J. E., Grachev, A. A., & Edson, J. B. (2003). Bulk parameterization of air–sea fluxes: Updates and verification for the COARE algorithm. *Journal of Climate*, 16(4), 571–591. [https://doi.org/10.1175/1520-0442\(2003\)016<0571:BPOASF>2.0.CO;2](https://doi.org/10.1175/1520-0442(2003)016<0571:BPOASF>2.0.CO;2)

Frenger, I., Gruber, N., Knutti, R., & Münnich, M. (2013). Imprint of southern ocean eddies on winds, clouds and rainfall. *Nature Geoscience*, 6(8), 608–612. <https://doi.org/10.1038/ngeo1863>

Frenger, I., Münnich, M., & Gruber, N. (2018). Imprint of southern ocean mesoscale eddies on chlorophyll. *Biogeosciences*, 15(15), 4781–4798. <https://doi.org/10.5194/bg-15-4781-2018>

Gaube, P., McGillicuddy, D. J., Jr., & Moulin, A. J. (2019). Mesoscale eddies modulate mixed layer depth globally. *Geophysical Research Letters*, 46(3), 1505–1512. <https://doi.org/10.1029/2018GL080006>

Hausmann, U., & Czaja, A. (2012). The observed signature of mesoscale eddies in sea surface temperature and the associated heat transport. *Deep Sea Research Part I: Oceanographic Research Papers*, 70, 60–72. <https://doi.org/10.1016/j.dsr.2012.08.005>

He, Q., Zhan, H., & Cai, S. (2020). Anticyclonic eddies enhance the winter barrier layer and surface cooling in the Bay of Bengal. *Journal of Geophysical Research: Oceans*, 125(10), e2020JC016524. <https://doi.org/10.1029/2020JC016524>

Itoh, S., & Yasuda, I. (2010). Water mass structure of warm and cold anticyclonic eddies in the western boundary region of the subarctic North Pacific. *Journal of Physical Oceanography*, 40(12), 2624–2642. <https://doi.org/10.1175/2010JPO4475.1>

L'Hégaret, P., Carton, X., Louazel, S., & Boutin, G. (2016). Mesoscale eddies and submesoscale structures of Persian Gulf Water off the Omani coast in spring 2011. *Ocean Science*, 12(3), 687–701. <https://doi.org/10.5194/os-12-687-2016>

Li, H., Xu, F., & Wang, G. (2022). Global mapping of mesoscale eddy vertical tilt. *Journal of Geophysical Research: Oceans*, 127(11), e2022JC019131. <https://doi.org/10.1029/2022JC019131>

Lin, Y., & Wang, G. (2021). The effects of eddy size on the sea surface heat flux. *Geophysical Research Letters*, 48(23), e2021GL095687. <https://doi.org/10.1029/2021GL095687>

Liu, X., Chang, P., Kurian, J., Saravanan, R., & Lin, X. (2018). Satellite-observed precipitation response to ocean mesoscale eddies. *Journal of Climate*, 31(17), 6879–6895. <https://doi.org/10.1175/JCLI-D-17-0668.1>

Liu, Y., Yu, L., & Chen, G. (2020). Characterization of sea surface temperature and air–sea heat flux anomalies associated with mesoscale eddies in the South China Sea. *Journal of Geophysical Research: Oceans*, 125(4), e2019JC015470. <https://doi.org/10.1029/2019JC015470>

McGillicuddy, D. J. (2015). Formation of intrathermocline lenses by eddy–wind interaction. *Journal of Physical Oceanography*, 45(2), 606–612. <https://doi.org/10.1175/JPO-D-14-0221.1>

Melnichenko, O., Amores, A., Maximenko, N., Hacker, P., & Potemra, J. (2017). Signature of mesoscale eddies in satellite sea surface salinity data. *Journal of Geophysical Research: Oceans*, 122(2), 1416–1424. <https://doi.org/10.1002/2016JC012420>

Moreton, S., Ferreira, D., Roberts, M., & Hewitt, H. (2021). Air–sea turbulent heat flux feedback over mesoscale eddies. *Geophysical Research Letters*, 48(20), e2021GL095407. <https://doi.org/10.1029/2021GL095407>

Moschos, E., Barboni, A., & Stegner, A. (2022). Why do inverse eddy surface temperature anomalies emerge? The case of the Mediterranean Sea. *Remote Sensing*, 14(15), 3807. <https://doi.org/10.3390/rs14153807>

Ni, Q., Zhai, X., Jiang, X., & Chen, D. (2021). Abundant cold anticyclonic eddies and warm cyclonic eddies in the global ocean. *Journal of Physical Oceanography*, 51(9), 2793–2806. <https://doi.org/10.1175/JPO-D-21-0010.1>

Pegliasco, C., Busché, C., & Faugère, Y. (2022). *Mesoscale eddy trajectory Atlas META3.2 delayed-time all satellites*. CNES. <https://doi.org/10.24400/527896/A01-2022.005>

Phillips, H. E., Tandon, A., Furue, R., Hood, R., Ummenhofer, C. C., Benthuisen, J. A., et al. (2021). Progress in understanding of Indian Ocean circulation, variability, air–sea exchange, and impacts on biogeochemistry. *Ocean Science*, 17(6), 1677–1751. <https://doi.org/10.5194/os-17-1677-2021>

Rai, S., Hecht, M., Maltrud, M., & Aluie, H. (2021). Scale of oceanic eddy killing by wind from global satellite observations. *Science Advances*, 7(28), eabf4920. <https://doi.org/10.1126/sciadv.abf4920>

Raj Parampil, S., Bharathraj, G. N., Harrison, M., & Sengupta, D. (2016). Observed subseasonal variability of heat flux and the SST response of the tropical Indian Ocean. *Journal of Geophysical Research: Oceans*, 121(10), 7290–7307. <https://doi.org/10.1002/2016JC011948>

Schott, F. A., & McCreary, J. P. (2001). The monsoon circulation of the Indian Ocean. *Progress in Oceanography*, 51(1), 1–123. [https://doi.org/10.1016/S0079-6611\(01\)00083-0](https://doi.org/10.1016/S0079-6611(01)00083-0)

- Seo, H., Subramanian, A. C., Song, H., & Chowdary, J. S. (2019). Coupled effects of ocean current on wind stress in the Bay of Bengal: Eddy energetics and upper ocean stratification. *Deep Sea Research Part II: Topical Studies in Oceanography*, 168, 104617. (Atmosphere-Ocean Dynamics of Bay of Bengal - Volume I). <https://doi.org/10.1016/j.dsr2.2019.07.005>
- Song, H., Marshall, J., Munro, D. R., Dutkiewicz, S., Sweeney, C., McGillicuddy, D. J., Jr., & Hausmann, U. (2016). Mesoscale modulation of air-sea CO<sub>2</sub> flux in drake passage. *Journal of Geophysical Research: Oceans*, 121(9), 6635–6649. <https://doi.org/10.1002/2016JC011714>
- Spall, M. A. (2000). Generation of strong mesoscale eddies by weak ocean gyres. *Journal of Marine Research*, 58(1), 97–116. <https://doi.org/10.1357/002224000321511214>
- Sun, W., An, M., Liu, J., Liu, J., Yang, J., Tan, W., et al. (2022). Comparative analysis of four types of mesoscale eddies in the Kuroshio-oyashio extension region. *Frontiers in Marine Science*, 9. <https://doi.org/10.3389/fmars.2022.984244>
- Thadathil, P., Muraleedharan, P. M., Rao, R. R., Somayajulu, Y. K., Reddy, G. V., & Revichandran, C. (2007). Observed seasonal variability of barrier layer in the Bay of Bengal. *Journal of Geophysical Research*, 112(C2). <https://doi.org/10.1029/2006JC003651>
- Trott, C. B., Subrahmanyam, B., Chaigneau, A., & Roman-Stork, H. L. (2019). Eddy-induced temperature and salinity variability in the Arabian Sea. *Geophysical Research Letters*, 46(5), 2734–2742. <https://doi.org/10.1029/2018GL081605>
- Varna, M., Jithin, A., & Francis, P. (2023). Characteristics and dynamics of mesoscale eddies in the eastern Arabian Sea. *Deep Sea Research Part II: Topical Studies in Oceanography*, 207, 105218. <https://doi.org/10.1016/j.dsr2.2022.105218>
- Vic, C., Rouillet, G., Capet, X., Carton, X., Molemaker, M. J., & Gula, J. (2015). Eddy-topography interactions and the fate of the Persian Gulf Outflow. *Journal of Geophysical Research: Oceans*, 120(10), 6700–6717. <https://doi.org/10.1002/2015JC011033>
- Villas Bôas, A. B., Sato, O. T., Chaigneau, A., & Castelão, G. P. (2015). The signature of mesoscale eddies on the air-sea turbulent heat fluxes in the South Atlantic Ocean. *Geophysical Research Letters*, 42(6), 1856–1862. <https://doi.org/10.1002/2015GL063105>
- Wunsch, C. (1999). Where do ocean eddy heat fluxes matter? *Journal of Geophysical Research*, 104(C6), 13235–13249. <https://doi.org/10.1029/1999JC900062>
- Yu, L. (2019). Global air–sea fluxes of heat, fresh water, and momentum: Energy budget closure and unanswered questions. *Annual Review of Marine Science*, 11(1), 227–248. <https://doi.org/10.1146/annurev-marine-010816-060704>
- Yu, L., & Jin, X. (2014a). Confidence and sensitivity study of the OAFflux multisensor synthesis of the global ocean surface vector wind from 1987 onward. *Journal of Geophysical Research: Oceans*, 119(10), 6842–6862. <https://doi.org/10.1002/2014JC010194>
- Yu, L., & Jin, X. (2014b). Insights on the OAFflux ocean surface vector wind analysis merged from scatterometers and passive microwave radiometers (1987 onward). *Journal of Geophysical Research: Oceans*, 119(8), 5244–5269. <https://doi.org/10.1002/2013JC009648>
- Yu, L., & Jin, X. (2018). A regime-dependent retrieval algorithm for near-surface air temperature and specific humidity from multi-microwave sensors. *Remote Sensing of Environment*, 215, 199–216. <https://doi.org/10.1016/j.rse.2018.06.001>
- Zhang, Z., Wang, W., & Qiu, B. (2014). Oceanic mass transport by mesoscale eddies. *Science*, 345(6194), 322–324. <https://doi.org/10.1126/science.1252418>
- Zhu, J., Zhang, Y., Cheng, X., Wang, X., Sun, Q., & Du, Y. (2022). Effect of mesoscale eddies on the transport of low-salinity water from the Bay of Bengal into the Arabian Sea during winter. *Geoscience Letters*, 9(1), 37. <https://doi.org/10.1186/s40562-022-00246-7>